

Turning the Tides on the Ultra-Faint Dwarf Spheroidal Galaxies: Coma Berenices and Ursa Major II¹

Ricardo R. Muñoz², Marla Geha², & Beth Willman³

ABSTRACT

We present deep CFHT/MegaCam photometry of the ultra-faint Milky Way satellite galaxies Coma Berenices (ComBer) and Ursa Major II (UMa II). These data extend to $r \sim 25$, corresponding to three magnitudes below the main sequence turn-offs in these galaxies. We robustly calculate a total luminosity of $M_V = -3.8 \pm 0.6$ for ComBer and $M_V = -3.9 \pm 0.5$ for UMa II, in agreement with previous results. ComBer shows a fairly regular morphology with no signs of active tidal stripping down to a surface brightness limit of $32.4 \text{ mag arcsec}^{-2}$. Using a maximum likelihood analysis, we calculate the half-light radius of ComBer to be $r_{\text{half}} = 74 \pm 4 \text{ pc}$ ($5.8 \pm 0.3'$) and its ellipticity $\epsilon = 0.36 \pm 0.04$. In contrast, UMa II shows signs of on-going disruption. We map its morphology down to $\mu_V = 32.6 \text{ mag arcsec}^{-2}$ and found that UMa II is larger than previously determined, extending at least $\sim 700 \text{ pc}$ (1.2° on the sky) and it is also quite elongated with an ellipticity of $\epsilon = 0.50 \pm 0.2$. However, our estimate for the half-light radius, $123 \pm 3 \text{ pc}$ ($14.1 \pm 0.3'$) is similar to previous results. We discuss the implications of these findings in the context of potential indirect dark matter detections and galaxy formation. We conclude that while ComBer appears to be a stable dwarf galaxy, UMa II shows signs of on-going tidal interaction.

Subject headings: dark matter – galaxies: dwarf - galaxies: individual (Coma Berenices, Ursa Major II) – Local Group

¹Based on observations obtained at the Canada-France-Hawaii Telescope (CFHT) which is operated by the National Research Council of Canada, the Institut National des Sciences de l'Univers of the Centre National de la Recherche Scientifique of France, and the University of Hawaii.

²Astronomy Department, Yale University, New Haven, CT 06520, USA (ricardo.munoz@yale.edu, marla.geha@yale.edu)

³Haverford College, Department of Astronomy, 370 Lancaster Avenue, Haverford, PA 19041, USA (bwillman@haverford.edu)

1. Introduction

For decades, only about a dozen dwarf galaxies were known to orbit the Milky Way. The majority of these systems corresponded to dwarf spheroidal (dSph) galaxies, the least luminous, but, by number, the dominant galaxy type in the present-day universe. However, over the last five years, and thanks to the advent of the Sloan Digital Sky Survey (SDSS; York et al. 2000) the field of dwarf galaxies in the Milky Way has been revolutionized. To date, fourteen new systems have been detected as slight overdensities in star count maps using the SDSS data (Willman et al. 2005a,b; Belokurov et al. 2006, 2007a, 2008, 2009; Zucker et al. 2006a,b; Sakamoto & Hasegawa 2006; Irwin 2007; Walsh et al. 2009). These recent discoveries have revealed a previously unknown population of “ultra-faint” systems which have extreme low luminosities, in some cases as low as $L_V \sim 300 L_\odot$ (Martin et al. 2008), and in average comparable (or lower) to those of Galactic globular clusters. However, spectroscopic surveys of the majority of these systems reveal kinematics and metallicities in line with those of dwarf galaxies (Kleyna et al. 2005; Muñoz et al. 2006; Simon & Geha 2007; Kirby et al. 2008; Koch et al. 2009; Geha et al. 2009).

Dynamical mass estimates of the ultra-faint galaxies based on line-of-sight radial velocities indicate that these galaxies are extremely dark matter dominated, with central mass-to-light ratios (M/L) as high as 1,000 in solar units. These systems are thus good laboratories to constrain cosmological models (e.g the ‘missing satellites problem’; Kauffmann et al. 1993; Moore 1999; Klypin et al. 1999; Simon & Geha 2007) and to study the properties of dark matter (Strigari et al. 2008; Kuhlen et al. 2008; Geha et al. 2009). However, these applications hinge critically on the assumption that the masses and density distributions in these systems are accurately known. Current mass estimates for the ultra-faint dwarfs are based on the assumption that the dynamical state of these systems have not been significantly affected by Galactic tides, and therefore that they are near dynamical equilibrium.

There is circumstantial evidence for past tidal disturbance in a number of these satellites based on morphological studies. Coleman et al. (2007) for instance, found the Hercules dSph to be highly elongated, with a major to minor axis ratio of 6:1, larger than for any of the “classical” dSphs, and argued for a tidal origin of this elongation. Belokurov et al. (2007a) reported fairly distorted morphologies for several of the new ultra-faint dwarfs, although Martin et al. (2008) showed that results based on low number of star may not be statistically significant because they suffer from shot noise. The strongest evidence for tidal interaction perhaps is for Ursa Major II, which appears to be broken into several clumps, lies close to the great circle that includes the Orphan Stream (Zucker et al. 2006b; Fellhauer et al. 2007) and shows a velocity gradient along its major axis (Simon & Geha 2007).

If dSphs galaxies are currently undergoing tidal stripping, or have in the past, then

kinematical samples are expected to be “contaminated” with unbound or marginally bound stars. This will impact subsequent dynamical modeling, often resulting in overestimated mass contents (Klimentowski et al. 2007; Lokas 2009). The degree of such contamination is a function of both the projection of the orbit along the line-of-sight and the strength of the tidal interaction. Therefore, even though tides do not affect appreciably the inner kinematics of dSphs until the latest stages of tidal disruption (e.g., Oh, Lin, & Aarseth 1995; Johnston et al. 1999; Muñoz et al. 2008; Peñarrubia et al. 2008), studies aimed at identifying the presence of tidal debris can help elucidate the dynamical state of these dwarf galaxies. Obvious tidal features around dSphs would indicate the presence of unbound stars and their effects on the derived masses would need to be investigated. Alternatively, a lack of clear detections in the plane of the sky would narrow the possibilities that kinematical samples suffer from contamination, although it would not automatically imply that an object has not been tidally affected. Tidal features could still exist but be aligned preferentially along the line-of-sight and thus be hard to detect.

Ultra-faint dwarf galaxies are useful probes of galaxy formation on the smallest scales (Madau et al. 2008; Ricotti et al. 2008). One of the outstanding questions related to their discovery is whether these galaxies formed intrinsically with such low luminosities, or whether they were born as brighter objects and attained their current luminosities through tidal mass loss. Current metallicity measurements (e.g., Kirby et al. 2008) support the former scenario. They show that the ultra-faint dwarfs are also the most metal poor of the dSphs, following the luminosity-metallicity trend found for the classical dSphs¹. On the other hand, if tidal features around these objects are firmly detected, it would clearly support the latter hypothesis.

Given the importance of the questions at hand, it is essential that we investigate the dynamical state of these satellites. Due to the extreme low luminosity of the ultra-faint dwarfs, and therefore low number of brighter stars available for spectroscopic studies, deep imaging is currently the only way to efficiently detect the presence of faint morphological features in the outskirts of these systems. We expect any tidal debris to be of very low surface brightness (Bullock & Johnston 2005) so that detecting it via integrated light is virtually impossible. However, these galaxies are sufficiently nearby to resolve individual stars. Thus, using matched-filter techniques it is possible to detect arbitrarily low surface

¹Simon & Geha (2007), using the same spectroscopic data but a different technique, reported systematically higher metallicities for the ultra-faint dwarfs than those of Kirby et al. (2008). The discrepancy is explained by the fact that the former study used the Rutledge et al. (1997) method that relies on the linear relationship between Ca II triplet equivalent widths and $[\text{Fe}/\text{H}]$, a technique now known to fail at very low metallicities.

brightness features (~ 35 mag arcsec $^{-2}$, Rockosi et al. 2002; Grillmair 2006).

In this article we present the results of a deep, wide-field photometric survey of the Coma Berenices (ComBer) and Ursa Major II (UMa II) dSphs, claimed to be two of the most dark matter dominated dSphs (Strigari et al. 2008), carried out with the MegaCam imager on the Canada-France-Hawaii Telescope. In §2, we present details about the observations and data reduction, as well as of artificial star tests carried out to determine our completeness levels and photometric uncertainties. In §3, we recalculate the structural parameters of these systems using a maximum likelihood analysis similar to that of Martin et al. (2008). In §4 we present the results of our morphological study. We discuss the statistical significance of our density contour maps and the robustness of our result to the variation of different parameters. We show that ComBer looks fairly regular in shape and find no signs of tidal debris down to a surface brightness limit of 32.4 mag arcsec $^{-2}$, whereas UMa II shows a significantly elongated and distorted shape, likely the result of tidal interaction with the Milky Way. Our discussion and conclusions are presented in §5 and §6, respectively.

2. Observations and Data Reduction

2.1. Observations

Observations of both ComBer and UMa II were made with the MegaCam imager on the Canada-France-Hawaii Telescope (CFHT) in queue mode. MegaCam is a wide-field imager consisting of 36 2048×4612 pixel CCDs, covering almost a full 1×1 deg 2 field of view with a pixel scale of 0.187"/pixel. UMa II was observed on nights between February and March of 2008, whereas ComBer was observed between April and May of 2008.

For each dSph, four different, slightly overlapping fields were observed for a total area coverage of nearly 2×2 deg 2 in the case of ComBer, and 1.4×2 deg 2 in the case of UMa II. In each field, the center of the dSph was placed in one of the corners so that, when combined, the galaxy is located at the center of the overlapping regions as shown in Figure 1. For each of the four fields, we obtained eleven 270s dithered exposures in Sloan g and eleven 468s dithered exposures in Sloan r in mostly dark conditions with typical seeing of 0.7 – 0.9". The dithering pattern was selected from the standard MegaCam operation options in order to cover both the small and large gaps between chips (the largest vertical gaps in MegaCam are six times wider than the small gaps).

2.2. Data Reduction and Astrometry

MegaCam data are pre-processed by the CFHT staff using the “Elixir” package (Magnier & Cuillandre 2004) prior to delivery. The goal is to provide the user with frames that are corrected for the instrumental signature across the whole mosaic. This pre-process includes bad pixel correction, bias subtraction and flat fielding. A preliminary astrometric and photometric solution is also included in the pre-processed headers.

The World Coordinate System (WCS) information provided with the data is only approximate, and we refine it using the freely available SCAMP² package as follows: Terapix SExtractor³ is run on all chips (SCAMP reads in the output files generated by SExtractor) and output files are written in the FITS-LDAC⁴ format. SCAMP is then run on all chips. SCAMP uses the approximate WCS information in the frames’ headers as a starting point, and then computes astrometric solutions using, in our case, the SDSS-Data Release 6 (DR6, York et al. 2000; Adelman-McCarthy et al. 2008) reference catalog which is automatically downloaded from the VizieR database. Typically, several hundred stars in common between each of our chips and SDSS are used to compute the astrometry and final solutions. In ComBer, fields have typical global astrometric uncertainties of $rms \sim 0.15''$, while for fields in UMa II they are slightly higher, with $rms \sim 0.2''$. The output from SCAMP is a FITS header file (one per processed frame), which is then used to update the WCS information for that given chip. The updated headers are then used to translate x and y positions into final equatorial coordinates.

2.3. Point Source Photometry

Prior to performing point-source photometry on our data, we split each mosaic frame into its 36 individual chips. To take full advantage of our 11 dithered exposures per field (and per filter), we test two different methods for carrying out the photometry.

²See <http://astromatic.iap.fr/software/scamp/>

³See <http://astromatic.iap.fr/software/sextractor/>

⁴LDAC stands for Leiden Data Analysis Center.

2.3.1. *ALLFRAME on Individual Exposures*

For the first method, we carry out our photometry running first DAOPHOT/Allstar on the individual, non-coadded frames and then running the ALLFRAME package on the resulting files as outlined in Stetson (1994). ALLFRAME performs photometry simultaneously on all 22 frames for a given field (11 per filter). DAOPHOT/Allstar are required prior to ALLFRAME to determine point spread function (PSF) solutions for each chip as well as to generate starlists for them individually. Optimum starlists to be used as input by ALLFRAME are obtained by cross matching the DAOPHOT/Allstar results for the individual frames using the DAOMATCH and DAOMASTER packages (Stetson 1993). These packages also provide reasonably good estimates of the offsets between dithered individual exposures necessary to run ALLFRAME. Final output files from ALLFRAME are then combined into a single catalog.

2.3.2. *DAOPHOT/ALLSTAR on Stacked Images*

In our alternative reduction method, we coadd all 11 exposures per filter for each of the 36 individual chips using the SWARP package⁵. SWARP uses the WCS information stored in the frames' headers to correct for shifts, small rotation between chips and distortions. However, since original WCS information in the headers is only approximate, we refine the astrometry (as described in §2.2) for all frames prior to combining. SWARP then coadds the frames and the DAOPHOT II/Allstar package is used to do point-source photometry on the stacked images.

Using artificial star tests described below, we determine that the ALLFRAME method (§2.3.1) yields slightly deeper and more accurate photometry and therefore we continue our data reduction and analysis using the catalog generated as described in the first part of this section.

2.3.3. *Photometric Calibration*

Finally, photometric calibration was carried out by comparison with the SDSS-Data Release 7 (DR7, Abazajian et al. 2009) catalog. We first match our final photometry with the SDSS stellar catalog. We typically found several hundred stars in common with SDSS

⁵See <http://astromatic.iap.fr/software/swarp/>

per chip. To determine zero point and color terms we only use stars with $18 < r < 21.5$ and $0.0 < g - r < 1.0$. The brighter limit is given by the saturation limit of our CFHT data. We then fit the equations:

$$g = g_{\text{instr}} + g_0 + g_1(g - r) \quad (1)$$

$$r = r_{\text{instr}} + r_0 + r_1(g - r) \quad (2)$$

where g_0 and r_0 are the zero points and g_1 and r_1 are the respective color terms. We do this for each chip individually in order to determine whether there are chip-to-chip variations. In all cases, we find that the chip-to-chip differences, for both zero points and color terms are lower than the uncertainties in the derived parameters, and therefore we combine the stars in all 36 chips to derive final zero point and color term values. We do this via a linear least-squares fit weighting by the respective uncertainties in the photometric magnitudes (as estimated by ALLFRAME) and rejecting 3σ outliers. We obtain zero point and color terms for each mosaic field independently (four per dSph, eight total). The resulting constants differ by less than 2% in all cases. Uncertainties in the zero points vary from $0.003 - 0.004$ mag whereas uncertainties in the color terms are of the order of ~ 0.005 .

2.4. Artificial Star Tests

Final photometric uncertainties and completeness levels are determined via artificial star tests. We first generate a fake color-magnitude-diagram (CMD) from which we will randomly select artificial stars. We populate the CMD with stars in the magnitude and color ranges of $18 < g/r < 28$ and $0.0 < (g - r) < 1.0$ respectively, with four times more stars in the $23 < g/r < 28$ range than in the brighter half of the CMD. We then select one of the 11 dithered exposures as our reference frame. In all cases we select the first exposure in the g filter for this purpose. The goal is to inject stars in all 22 frames (per chip) in the same fake RA and DEC positions in order to mimic real observations. Artificial stars are then randomly selected from the fake CMD and are injected into the reference frame in a uniform grid with a spacing of 40 pixels in both the x and y directions. Using the refined astrometric solution calculated by SCAMP we convert the x and y positions of the artificial stars into RA and DEC coordinates which are then converted back to x and y positions, but in the reference frame of the other exposures. Care is taken so that all the stars fall

in the common area between the 22 different exposures. In the end, nearly 3,950 stars are introduced per chip. We repeat this procedure ten times to improve our statistics, each time randomly offsetting the grid’s zero-point position in x and y . We then carry out photometry on the artificial stars using the ALLFRAME method in the exact same manner as we did for the science frames.

We perform this test on only one chip per mosaic frame due to computational constraints, for a total of four chips in each dSph. Since each of these fields was observed under slightly different seeing and darkness conditions, their respective magnitude limits are also slightly different. Thus, to set conservative overall completeness levels we select the values from our “shallowest” field in each dSph as our final numbers. We find that this represents a better choice than determining our limits from our combined artificial star’s photometry for all four chips. In the latter case, the deepest fields dominate the results. The 50% and 90% overall completeness levels of our photometry thus correspond to $g = 25.8$ and 25.2 and $r = 25.4$ and 24.75 , respectively, for our ComBer fields, and $g = 26.0$ and 25.4 and $r = 25.5$ and 24.9 , respectively, for UMa II. Figure 2 shows the resulting completeness levels.

In order to clean our catalogs of galaxy interlopers and other, non-stellar detections, we apply cuts using DAOPHOT’s sharpness (*sharp*) and χ parameters. To define appropriate cuts, we fit third-degree polynomials to the χ and *sharp* distributions, as functions of g magnitude, obtained from the artificial star tests. After applying these cuts to both our photometric catalog and artificial star photometry our 90% completeness levels drop to $g = 24.8$ and $r = 24.4$ for ComBer and $g = 24.9$ and $r = 24.5$ for UMa II.

In Figures 3 and 4, we show color-magnitude-diagrams (CMD) for the central regions of both galaxies, including 90% completeness levels. In both cases, we reach at least three magnitudes below the main sequence turn-off of these systems, improving by roughly an order of magnitude, with respect to the original SDSS photometry, the number of likely members of each galaxy. Photometric uncertainties as a function of magnitude were derived by taking the difference between the artificial star’s actual and measured magnitude and are shown as error bars in Figures 3 and 4.

3. Results

3.1. Structural Parameters

Our photometric catalogs for both ComBer and UMa II contain an order of magnitude more stars than the SDSS photometry, and thus provide us with an excellent opportunity to re-estimate the structural properties of these systems. Martin et al. (2008) carried out a

comprehensive analysis of the structural parameters of all the ultra-faints using the original SDSS photometry. However, in the cases of ComBer and UMa II, owing to their very low luminosities ($M_V \sim -4$), only about 100 and 300 stars were found to belong to the respective galaxy and therefore the derived parameters (and morphologies) suffer from significant uncertainties due to low numbers statistics.

For each galaxy, we re-calculate the photometric center (α_0, δ_0), ellipticity (ϵ), position angle (θ), half-light radius⁶ (r_{half}) and background density (Σ_b). We try three different density profiles, exponential, Plummer (Plummer 1911) and empirical King (King 1962), and obtain structural parameters for all three:

$$\Sigma_{exp}(r) = \Sigma_{0,E} \exp\left(-\frac{r}{r_E}\right) \quad (3)$$

$$\Sigma_{Plummer}(r) = \Sigma_{0,P} \left(1 + \frac{r^2}{r_P^2}\right)^{-2} \quad (4)$$

$$\Sigma_{King}(r) = \Sigma_{0,K} \left(\left(1 + \frac{r^2}{r_c^2}\right)^{-\frac{1}{2}} - \left(1 + \frac{r_t^2}{r_c^2}\right)^{-\frac{1}{2}} \right)^2 \quad (5)$$

where r_E and r_P are the exponential and Plummer scale lengths and r_c and r_t correspond to the King core and tidal radii respectively. The exponential scale length is related to the half-light radius by the relation $r_{\text{half}} = 1.68 \times r_E$ while in the case of the Plummer profile, r_P is equivalent to r_{half} .

We have followed a procedure similar to the one outlined in Martin et al. (2008) which relies on a maximum likelihood (ML) analysis of the data to constrain the structural parameters. The basic idea of the method is as follows: We assume that the positions of the stars are well represented by a given density profile (one of the three mentioned above) which is, in turn, well described by a set of parameters p_1, p_2, \dots, p_j . We then maximize a function of the form:

$$L(p_1, p_2, \dots, p_j) = \prod_i l_i(p_1, p_2, \dots, p_j) \quad (6)$$

where $l_i(p_1, p_2, \dots, p_j)$ is the probability of finding the datum i given the set of parameters p_1, p_2, \dots, p_j . In the case of an exponential profile, this function takes the form:

⁶In the case of King profiles we calculate their r_{core} and r_{tidal} .

$$l_i(p_1, p_2, \dots, p_j) = S_0 \exp\left(-\frac{r_i}{r_E}\right) + \Sigma_b \quad (7)$$

where S_0 , r_i and r_E are expressed in terms of the structural parameters we want to determine.

In practice, we look for a global maximum $L(\hat{p}_1, \hat{p}_2, \dots, \hat{p}_j)$ by searching the j -dimensional parameter space. In our case, the parameter space is 6^{th} -dimensional, with the free parameters α_0 , δ_0 , ϵ , θ , r_{half} and Σ_b . In the case of a King profile, we fix the background density using the value obtained for the Plummer profile because of a degeneracy between Σ_b and the King tidal radius. To find a solution, we use the method described in Sand et al. (2009) which relies on the amoeba simplex algorithm (Press 1988) to search the parameter space. This method is somewhat sensitive to the specified region of parameter space to be searched (i.e. the initial guess and allowed range for the parameters) but it runs considerably faster than using an iteratively refined grid. In order to derive uncertainties for the structural parameters, we carry out 10,000 bootstrap (resampling with replacement) realizations of our data. The distribution of a given parameter is well described by a Gaussian with only minor deviations in some cases (King core and tidal radii in particular), and therefore we fit Gaussian functions and report their mean and standard deviation as the mean and $1-\sigma$ uncertainty for a given parameter.

To facilitate comparison with previous studies, we first compare the results of our algorithm when applied to the SDSS data with those derived by Martin et al. (2008). To mimic their star selection procedure as closely as possible, we select stars within 1 degree from the satellites' centers, impose the conditions that $r < 22.0$, $g < 22.5$ and, additionally, that stars live near the M92 fiducial line shifted to the distance of the respective dwarf satellite. We perform the comparison only for the exponential profile. For both galaxies, the resulting structural parameters are in very good agreement. However, since we determine our parameters via a bootstrap analysis, our derived uncertainties are significantly larger. Martin et al. (2008) did not perform a bootstrap analysis of their data and estimated their uncertainties using the statistical properties of the L function. However, as shown in the same study, statistical fluctuations due to the low number of stars in these dSphs can dramatically affect the morphology as well as the best-fitting parameters and therefore we regard our uncertainties as more realistic.

We then apply the ML algorithm to our dataset. We select stars above the 90% completeness levels and within a region around the main sequences of these objects (in order to improve the signal to noise ratio of dSph versus Milky Way foreground stars). For this purpose, we use an isochrone for a population 13 Gyr old and $[\text{Fe}/\text{H}] = -2.27$ ($Z = 0.0001$) from Girardi et al. (2004) and define a region around the main sequences by the condition

that stars have to lie within 0.075 mag from the isochrone. We varied this distance between 0.050–0.100 mag and found no significant changes in the final parameters. We note that we do not match the isochrone to the blue edge of the main sequence as it is customary when isochrone matching is used to derive star cluster properties, but instead place the isochrone so that it goes through the middle of the main sequences. For ComBer, our ML method yields a $r_{\text{half}} = 5.8 \pm 0.3$ arcmin, an ellipticity $\epsilon = 0.36 \pm 0.04$ and a position angle $\theta = -67.0 \pm 3.6$ for the case of an exponential profile with the parameters derived for the other profiles being very similar. In the case of UMa II we find $r_{\text{half}} = 14.1 \pm 0.3$ arcmin, $\epsilon = 0.50 \pm 0.02$ and $\theta = -74.8 \pm 1.7$. The final sets of structural properties for both ComBer and UMa II are presented in Table 1.

This exercise also allows us to compare the results obtained from both our CFHT photometry and the shallower SDSS data. As it was pointed out by Sand et al. (2009) in their work on the Hercules dSph, we find relatively good agreement between the results obtained with both datasets, but our photometry allows us to place much tighter constraints on the derived structural properties. This is not surprising given that our deeper photometric database is less sensitive to shot-noise effects that plague the shallower SDSS data. Figure 5 illustrates this point. In this figure we show the distribution of four structural parameters for ComBer, α_0 , δ_0 , r_{half} and ϵ for all 10,000 bootstraps and for both datasets where the smaller uncertainties derived with the CFHT data are evident.

In Figures 6 and 7a we show background subtracted density profiles for both satellites with the best exponential, Plummer and King models overplotted. These are not fits to the binned data points, but are models constructed with the best parameters found via the ML method. As it can be seen, in the case of ComBer, both the exponential and King profiles are adequate descriptions of the data, with the Plummer profile being perhaps a less adequate one. The case of UMa II is quite different. Neither profile does a good job matching the data. In fact, as shown in Figure 7b, the data are better matched by a shallower inner power law ($\gamma = -0.96$) and a steeper one in the outer parts ($\gamma = -2.40$) reminiscent of the density profile derived by Grillmair (2009) for the Boötes III stellar overdensity or the inner power law shown by the tidally stripped Palomar 5 (Pal 5) globular cluster (Odenkirchen et al. 2003). This result is consistent with a scenario wherein UMa II has been significantly tidally stripped, as suggested by Zucker et al. (2006b). We will explore this possibility in more depth in §4.

3.2. Absolute Magnitude

We estimate the absolute total magnitudes of ComBer and UMa II following a procedure similar to that outlined by Walsh et al. (2008). This method relies solely on the number of stars belonging to the galaxy, and not on their individual magnitudes. As pointed out by Martin et al. (2008), Walsh et al. (2008) and Sand et al. (2009), the extreme low luminosity of the ultra-faint galaxies and therefore the low number of stars they contain, make traditional methods, like the addition of fluxes from individual stars, too sensitive to the inclusion (or exclusion) of potential members (outliers). Adding or subtracting a few red-giant-branch stars (with absolute magnitudes as bright as $M_V = -4.8$ for a metallicity of $[\text{Fe}/\text{H}] \sim -2.5$) can significantly alter the total luminosity measurement in these cases. We therefore follow the method briefly described below.

We first assume that the stellar populations of both systems are mainly comprised by old, metal-poor stars, and therefore are well described by a single population. We can then model that population with a theoretical luminosity function to help estimate its luminosity. For this exercise, we adopt luminosity functions from Girardi et al. (2004) for a population 13 Gyr old and with $Z = 0.0001$ (which corresponds to $[\text{Fe}/\text{H}] = -2.27$). This assumption is reasonable in light of the metallicity measurements by Kirby et al. (2008) who show that both dwarf galaxies have mean metallicities around $[\text{Fe}/\text{H}] = -2.5$. In addition, we use theoretical luminosity functions computed using two different initial mass functions (IMF): a Salpeter (1955) with cutoff at $0.01 M_\odot$ and a Chabrier (2001) log-normal.

The theoretical luminosity function gives us the relative number of stars in magnitude bins, which can be integrated to obtain the total flux down to a given magnitude limit. One of the parameters we determine using the ML algorithm is the background surface density Σ_b which is related the number of stars N_* that belong to the galaxies by:

$$N_* = N_{\text{total}} - A\Sigma_b \quad (8)$$

where N_{total} is the total number of stars used to derive the structural parameters and A represents the total area of our fields. We use this N_* to normalize the theoretical luminosity function. By integrating the luminosity function and correcting by this normalization factor we obtain the actual flux corresponding to our galaxies down to the respective magnitude limits. To account for the light contributed by stars fainter than this limit, we add the remaining normalized integrated flux.

As mentioned above, this method differs from traditional ones, and our derived luminosities are conceptually different from those derived for brighter galaxies. In our method,

two different galaxies comprised of the same population and with exactly the same number of stars will always have the same luminosity. However, in practice this will most likely not be the case as one might expect galaxies with similar populations to show an intrinsic spread in luminosities even if they have the same number of stars. To account properly for this we estimate uncertainties in our derived absolute magnitudes by carrying out a bootstrap analysis. The procedure is as follows: We treat the theoretical luminosity function used to calculate the luminosities as a cumulative probability function (down to our 90% completeness levels) of the number of stars expected as a function of magnitude. We then randomly draw a number N_* of stars from the luminosity function and add their fluxes. We do this 10,000 times. Using this method, for the case of a Salpeter IMF we find, for ComBer, $M_V = -3.8 \pm 0.6$ (after using $V - r = 0.16$ from Girardi et al. 2004). For UMa II we obtain $M_V = -3.9 \pm 0.5$. For the second choice of IMF we obtain $M_V = -3.8 \pm 0.6$ for ComBer and $M_V = -4.0 \pm 0.6$ for UMa II. The uncertainties quoted here do not include the uncertainties in the distance to this objects. To test further whether our method yields reliable values, we apply it to SDSS data selected in the same way as described in §3.1. For a choice of a Salpeter or log-normal IMF our results are almost identical to those of Martin et al. (2008) but as in the case of deriving structural parameters our uncertainties are larger.

4. Morphology

A main goal of this study is to re-assess to what extent Galactic tides may be affecting the structure of ComBer and UMa II. Ever since the early numerical simulations of disrupted satellites by Piatek & Pryor (1995) and Oh, Lin, & Aarseth (1995), the observed elongation of dSph galaxies have been associated with the degree of their tidal interaction with the Milky Way⁷. In §3.1 we found that ComBer is slightly elongated ($\epsilon = 0.36$) roughly along the direction of the Galactic center (shown by the solid line in Figure 8). UMa II, on the other hand, is much more elongated, with $\epsilon = 0.5$ but its elongation is in the east-west direction, nearly perpendicular to the direction of the Galactic center⁸ (UMa II has galactic coordinates of $[l,b]=[152.5, 37.5]$). While alignment with the Galactic center is expected in intrinsically elongated satellites, it is not a sufficient condition to infer active tidal stripping in the case of ComBer. Tides can still affect a system without necessarily stripping stars off

⁷The same studies, and more recently Muñoz et al. (2008) have pointed out that this is not usually the case. Intrinsically spherical satellites are tidally elongated only when the satellite has become nearly unbound.

⁸This does not preclude UMa II from being elongated along the direction of the Galactic center, but such elongation would be mostly along the line-of-sight and therefore very difficult to detect.

of that system (C. Simpson & K. Johnston, in preparation).

The quality of our photometric data, which reach at least three magnitudes below the main sequence turn-off in both galaxies, allows us to address the tidal stripping question more directly by studying the morphology of these satellites, this time much more reliably than in previous studies. To look for potential tidal features, we create smoothed isodensity contour maps. The photometric catalogs used to create these maps are the same as those we used to derive structural parameters, and include all star-like objects (i.e., after *sharp* and χ cuts) down to our 90% completeness levels that live in a region around the main sequence as defined in §3.1. To make the maps, the positions of the stars are binned into $40'' \times 40''$ bins which are subsequently spatially smoothed with an exponential filter of scale $2'$. Other reasonable bin sizes and exponential scales were tried as well, with no significant change in the overall results.

4.1. Coma Berenices

Figure 8 shows the resulting map for ComBer. This object shows fairly regular contours similar to those found using SDSS photometry (Belokurov et al. 2007a) but at a much higher statistical significance. We do not detect signs of potential tidal debris down to the 3σ isodensity contour level (the lowest one shown in Fig. 11) which corresponds to a surface brightness of ~ 32.4 mag arcsec $^{-2}$. The lack of significant elongation, clumpiness or irregularities in the morphology of ComBer indicate that it is unlikely that it is currently being significantly affected by tides. This, coupled with the kinematics of ComBer measured by Simon & Geha (2007) and the corresponding mass derivation, supports the interpretation that ComBer is in fact a stable dwarf galaxy. Even if ComBer is being tidally perturbed at levels below our detection limits, such low-level effects are not likely to alter its inner kinematics appreciably (e.g., Read et al. 2006; Muñoz et al. 2008; Peñarrubia et al. 2008).

We note that our countour maps do not show the actual smoothed surface brightness contours, but instead show “significance contours”, i.e, for each dwarf, we calculate the mean surface density and its standard deviation in areas away from the region dominated by the galaxy (background density), and plot the background-subtracted local density divided by the standard deviation. If the values of pixels in our surface density map are well described by a Gaussian distribution, then the standard deviation used here would measure precisely how significant our features are in terms of σ values. However, the distribution of pixels will, most likely, not be well described by a Gaussian, and therefore we need an experiment to determine the true significance of features in our data. To do this we first randomize the position of the stars, but leave the photometry untouched. We then select stars photometrically and

generate smoothed density maps in the same way as we do for the actual data. When we perform this test, we find that 3σ overdensities randomly scattered across the field are not uncommon, but higher significance features are very rare. We therefore conclude that isolated 3σ features detected in our real maps are very likely random noise and do not reflect potential tidal features.

To assess both the robustness of the overall shape of ComBer and the significance of apparent substructure in its outer density contours, specifically a hint of elongation in the northeast-southwest direction, we carry out a different test. In this case, we bootstrap our photometric samples (as opposed to randomly assign positions to the stars) and redo the maps. Figure 9 shows eight different bootstrap realizations of the data. It can be inferred from the figure that hints of substructure in the outer parts of ComBer are not statistically significant, but the overall shape and structure of this system are well established with our data. This is not surprising, given the improvement in the number of stars that belong to the satellite achieved with our photometry.

We conclude that ComBer is unlikely to be significantly affected by Galactic tides and therefore it represents a solid case of a stable dwarf galaxy whose characteristic size is smaller than ~ 120 pc.

4.2. Ursa Major II

In contrast to the regular morphology of ComBer, UMa II looks entirely different. Figure 10 shows its isodensity contour map, where the 3σ contours are equivalent to 32.6 mag arcsec $^{-2}$. Our photometry confirms previous findings that UMa II is highly elongated and it shows that UMa II is larger than previously reported, extending at least three times beyond its measured half-light radius, or nearly 700 pc ($\sim 1.2^\circ$) on the sky. More striking perhaps, is the fact that contours of UMa II looks more like a boxy-like system than an elliptical one. Only the very inner parts of UMa II resemble a spheroidal object.

In Figure 10 we also show the best-fit orbit derived for UMa II by Fellhauer et al. (2007), based on the assumption that it is the progenitor of the “Orphan Stream” (Zucker et al. 2006b; Belokurov et al. 2007b). This shows that the observed east-west elongation of UMa II does not match the predicted direction from the model, although this is not enough to rule out a connection between the two systems.

To assess the statistical significance of our results we carry out the same tests we described in section §4.1. We find that remaking the surface density maps after randomly assigning coordinates to the stars yields identical results as in the ComBer case, namely,

that isolated 3σ features are likely background noise but higher significance ones are real. Likewise, making contour maps after bootstrapping the data shows that the overall shape of UMa II is fairly well established and is insensitive to resampling. We illustrate this in Figure 11 where we show isodensity contours for eight different bootstrap realizations of our UMa II data.

Zucker et al. (2006b) found tentative evidence that UMa II might be broken into several clumps (see their Figure 1). Our contour map for this object does not show statistically significant substructure. However, we are able to reproduce this results if we make contour maps use only stars brighter than $g = 23$. We regard the presence of substructure in the inner parts of UMa II as statistical fluctuations in its density due to low number of stars.

Another of the ultra-faints that looks similarly elongated as UMa II is the Hercules dSph. A recent study of this object by Sand et al. (2009), who use deep photometry obtained with the Large-Binocular-Telescope (LBT), show that Hercules has an ellipticity $\epsilon = 0.67$ and extends at least 500 pc ($\sim 13'$ on the sky). We measured an ellipticity $\epsilon = 0.5$ for UMa I, but while this object resembles Hercules in this regard, UMa II's morphology is even more irregular.

5. Discussion

Our understanding of the ultra-faint Milky Way satellites hinge on having reliable morphologies and robust structural parameters. Tidal disruption can result in disturbed morphologies and tidal features which can be very low surface brightness, yet have a profound affect on the interpretation of a given object. Deep photometry is the only means to assess the presence or absence of faint tidal structure. In the absence of complete disruption, well determined sizes and luminosities are critical in calculating the total mass of a system. Our main goal in this paper is to search for signs of tidal features and determine structural parameters around the Milky Way satellites ComBer and UMa II. Our r - and g -band CFHT photometry reaches three magnitudes below the main sequence turn-off in these systems, corresponding to stars which are two to three magnitudes fainter than currently accessible to spectroscopic studies.

We achieve similar surface brightness limits for both ComBer and UMa II (~ 32.5 mag arcsec $^{-2}$), yet find very different morphologies for these two ultra-faint satellites. As seen in Figures 8 and 9, ComBer is remarkably regular and devoid of potential tidal features, in stark contrast to the elongated and irregular structure seen in UMa II. Since low number of stars can produce spurious features and/or shapes that can later be interpreted as signs of tidal

stripping (Martin et al. 2008), we have outlined in §4.1 two tests which demonstrated the robustness of our maps. We show that while the 3σ contours in these figures lack statistical significance, all higher σ contours are robust to resampling and should be regarded as a solid result.

ComBer is remarkably regular and devoid of morphological features potentially due to tidal debris down to a surface brightness level of $32.4 \text{ mag arcsec}^{-2}$. We have found a slight elongation in the direction toward the Galactic center but no discernible irregularities are visible. We cannot of course completely rule out the presence of unbound debris at fainter surface brightnesses, but, if present, it should reflect only mild, low-level tidal effects. Similarly, we cannot rule out the presence of tidal tails along the line-of-sight. In the kinematic survey of ComBer, Simon & Geha (2007) report a velocity dispersion for this object of $4.6 \pm 0.8 \text{ km s}^{-1}$ with only one possible interloper star beyond 3σ of the velocity distribution. This suggests against the presence of tidal debris along the line of sight. In the absence of evidence to the contrary, we conclude that ComBer is in dynamical equilibrium, and therefore current mass determinations should be robust.

Simon & Geha (2007) also report that radial velocity members of ComBer near the main sequence turn-off lie in a broader color region than the other ultra-faint dwarfs in their sample, which they attribute to the effects of multiple stellar populations of different ages and metallicities. We have investigated this and find that this spread is a reflection of larger photometric errors in the shallower SDSS data. We will further investigate the stellar populations of the two objects presented here in a separate paper.

In contrast to ComBer, UMa II shows signs of disequilibrium. The contours of UMa II are elongated, irregular and extend for at least 1.2° , three times its r_{half} . Only the very inner core of UMa II looks somewhat spheroidal. Unlike the case of most other dSphs, UMa II’s stellar density distribution is not well matched by any of the commonly used density profiles (King, Plummer or exponential), and instead it is better matched by two power laws. Several studies (e.g., Johnston et al. 1999; Muñoz et al. 2008; Peñarrubia et al. 2009) show that a dwarf satellite initially in a Plummer or King configuration develops a power law component in the outer parts as tidal debris is stripped by the Milky Way. However, they also show that the inner parts of the satellite retain a core-like density until the very latest stages of tidal disruption. The lack of a proper core in the stellar density profile of UMa II may be an indication that this system is in fact in the throes of destruction. Another way to assess qualitatively to what extent UMa II may have been tidally affected, is by comparing the “break” in its density profile⁹ to those of other well-studied disrupting objects such as

⁹By “break” we mean the inflection point where the inner density profile transitions into a power law due

Pal 5 or the Sagittarius (Sgr) dSph. These objects show a clear “break” in their density distributions around the region where tidal debris is being stripped. In the case of Pal 5 this happens at a surface density relative to the central one of $\Sigma_{N,0}/\Sigma_{\text{break}} \sim 100$ whereas for Sgr this value is closer to 200. If for UMa II we take the point where the inner power law changes slope as the “break” point, we obtain $\Sigma_{N,0}/\Sigma_{\text{break}} \sim 25$, higher than for Pal 5 and Sgr. In addition, this break in UMa II occurs relatively closer to the center than in these two systems, at a break radius $r_b \approx 2 \times r_{\text{half}}$ compared to $r_b \approx 4 \times r_{\text{half}}$ for the latter. All these observations further support a tidal scenario for UMa II.

Simon & Geha (2007) detect a velocity gradient along the major axis of UMa II, measuring an $8.4 \pm 1.4 \text{ km s}^{-1}$ velocity difference between in eastern and western halves of this object– in the same direction as the elongation seen in our deep photometry. They also point out that the UMa II’s velocity dispersion of $6.7 \pm 1.4 \text{ km s}^{-1}$ is an outlier in the observed trend of lower velocity dispersion with decreasing luminosity followed by other Galactic dwarf galaxies (see their Figure 10a). Given UMa II’s absolute magnitude of $M_V = -3.93$, a value of $3\text{--}4 \text{ km s}^{-1}$ would be more in line with the observed trend. One possibility to explain this observation is that the velocity dispersion of UMa II has been inflated by Galactic tides. We note however that these observations are limited to a small region inside r_{half} of the system. Despite the observational evidence discussed above in favor of the tidal stripping of UMa II, our current data set does not allow us to conclude that this object is completely unbound or out of dynamical equilibrium. Kinematical data in outer regions are required to determine more precisely the nature of UMa II and to further explore its possible association with the Orphan Stream.

In the context of the galaxy versus cluster issue raised by Gilmore et al. (2007, 2008), our findings (or lack thereof) imply that ComBer is solidly situated in the gap (in M_V versus r_{half} space) between star clusters and dwarf galaxies, and likely cannot be explained away as an evaporating cluster or dissolving dwarf galaxy. Metallicity measurements support this scenario. While our photometric work presented here show that the stellar content of ComBer (and UMa II) is consistent with being dominated by a very metal poor population of $[\text{Fe}/\text{H}] \sim -2.3$ (see Figs. 3 and 4), a metallicity unusually low even for the most metal poor globular clusters, detailed spectroscopic studies reveal even more extreme numbers. Kirby et al. (2008) report a mean metallicity for both ComBer and UMa II of $[\text{Fe}/\text{H}] \sim -2.5$ which falls squarely on the luminosity-metallicity relationship found for galaxies. Frebel et al. (2009) report high resolution abundances for three stars in ComBer with metallicities as low as $[\text{Fe}/\text{H}] \sim -2.9$, which is more metal poor than any of the Galactic

to the presence of tidal debris.

globular clusters. In addition, both studies show a metallicity spread of 0.6 dex in this dSph, typical of a dwarf galaxies. The same argument can be invoked to argue that UMa II is a disrupting dwarf galaxy as opposed to a dissolving star cluster.

6. Conclusions

We have carried out a deep, wide-field photometric survey of the Coma Berenices and Ursa Major II dwarf spheroidal galaxies using the MegaCam Imager on CFHT, reaching down to $r \sim 25$ mag, more than three magnitudes below the main sequence turn-offs of these Galactic satellites. This increases roughly by an order of magnitude, with respect to the original SDSS photometry, the number of stars that belong to the respective galaxies and that are available determination of their structural properties and for morphological studies.

Our results can be summarized as follows:

1. We used a maximum likelihood analysis similar to the one used by Martin et al. (2008) and Sand et al. (2009) to calculate structural parameters for three different density profiles: King, Plummer and exponential. We find characteristic sizes of $r_{\text{half}} = 74 \pm 4$ pc ($5.8 \pm 0.3'$) and 123 ± 3 pc ($14.1 \pm 0.3'$) for ComBer and UMa II respectively (from the exponential profile). Our results provide much tighter constraints on these structural parameters than possible with previous datasets, but are consistent with earlier determinations using SDSS photometry.

2. We have re-calculated the total luminosities for both systems and find, for ComBer $M_V = -3.8 \pm 0.6$ and for UMa II $M_V = -3.9 \pm 0.5$ (for a choice of Salpeter IMF), in very good agreement with previous results, confirming that ComBer and UMa II are among the faintest of the known dwarf satellites of the Milky Way. We have also used a Chabrier (2001) IMF but the results remain virtually unchanged.

3. We have found that ComBer shows a fairly regular morphology with no clear detection of potential stripped material down to a surface brightness of 32.4 mag arcsec $^{-2}$. Additionally, its number density profile is reasonably well matched by a choice of either King, Plummer or exponential profile. We thus conclude that ComBer is likely a stable dwarf galaxy which would make it one of the most dark matter dominated of the dSph systems.

4. We have also studied the morphology of UMa II and find that, unlike ComBer, it shows signs of being significantly disrupted. UMa II is larger than previously determined, extending at least ~ 700 pc (1.2° on the sky) and it is also quite elongated. Its density

profile and overall shape resemble a structure possibly in the latest stages of tidal destruction. Furthermore, its number density profile is not well matched by neither of the three profiles we tried and it is much better described by two power laws, further supporting a tidal scenario.

5. The overall 2D surface density distributions of both systems are not affected by shot-noise and are therefore robust. We find no evidence for isolated tidal debris beyond the main bodies of ComBer and UMaII to our surface brightness limits of 32.4 and 34.8 mag arcsec⁻², respectively.

Deep, wide-field imaging of the recently discovered ultra-faint galaxies currently lags behind spectroscopic observations of these objects. We show in this paper that high quality, deep photometry is an equally important tool in studying the dynamical state of the ultra-faint dwarfs. These data can also be used to constrain the star formation histories of ComBer and UMaII which we will explore in a future contribution.

We acknowledge David Sand, Josh Simon and Gail Gutowski for useful discussions and Peter Stetson for graciously providing copies of DAOPHOT and ALLFRAME. M.G and B.W. acknowledge support from the National Science Foundation under award number AST-0908752.

REFERENCES

- Abazajian, K. et al. 2009, ApJS, 182, 543
- Adelman-McCarthy, J. K., et al. 2008, ApJS, 175, 297
- Belokurov, V. et al. 2006, ApJ, 647, L111
- Belokurov, V. et al. 2007a, ApJ, 654, 897
- Belokurov, V. et al. 2007b, ApJ, 658, 337
- Belokurov, V. et al. 2008, ApJ, 686, L83
- Belokurov, V. et al. 2009, MNRAS, 397, 1748
- Bullock, J., & Johnston, K. V. 2005, ApJ, 635, 931
- Chabrier, G. 2001, ApJ, 554, 1274
- Coleman, M. G. et al. 2007, ApJ, 668, L43
- Fellhauer, M. et al. 2007, MNRAS, 375, 1171

- Frebel, A., Simon, J. D., Marla, G., & Willman, B. 2009, *ApJ*, *submitted*, arXiv:0902.2395
- Geha, M., Willman, B., Simon, J. D., Strigari, L. E., Kirby, E. N., Law, D. R., & Strader, J. 2009, *ApJ*, 692, 1464
- Gilmore, G., Wilkinson, M. I., Wyse, R. F. G., Kleyana, J. T., Koch, A., Evans, N. W., & Grebel, E. K. 2007, *ApJ*, 663, 948
- Gilmore, G. et al. 2008, in Kodama T., Yamada T., Aoki K., eds, ASP Conf. Ser. Vol. 399, Panoramic Views of Galaxy Formation and Evolution. Astron. Soc. Pac., San Francisco, p. 453
- Girardi, L., Grebel, E. K., Odenkirchen, M., & Chiosi, C. 2004, *A&A*, 422, 205
- Grillmair, C. J. 2006, *ApJ*, 651, 167
- Grillmair, C. J. 2009, *ApJ*, 693, 1118
- Irwin, M. J. et al. 2007, *ApJ*, 656, L13
- Johnston, K. V., Sigurdsson, S., & Hernquist, L. 1999, *MNRAS*, 302, 771
- Kauffmann, G., White, S. D. M., & Guiderdoni, B. 1993, *MNRAS*, 261, 201
- King, I. 1962, *AJ*, 67, 471
- Kirby, E. N., Simon, J. D., Geha, M., Guhathakurta, P., & Frebel, A. 2008, *ApJ*, 685, L43
- Kleyana, J. T., Wilkinson, M. I., Evans, N. W., & Gilmore, G. 2005, *ApJ*, 630, L141
- Klimentowski, J., Lokas, E. L., Kazantzidis, S., Prada, F., Mayer, L., & Mamon, G. A. 2007, *MNRAS*, 378, 353
- Klypin, A., Kravtsov, A., V., Valenzuela, O., & Prada, F. 1999, *ApJ*, 522, 82
- Koch, A. et al. 2009, *ApJ*, 690, 453
- Kuhlen, M., Diemand, J., & Madau, P. 2008, *ApJ*, 686, 262
- Lokas, E. L. 2009, *MNRAS*, 394, 102
- Madau, P., Diemand, J., & Kuhlen, M. 2008, *ApJ*, 679, 1260
- Magnier, E. A., & Cuillandre, J.-C. 2004, *PASP*, 116, 449
- Martin, N. F., de Jong, J. T. A., & Rix, H.-W. 2008, *ApJ*, 684, 1075

- Moore, B., Ghigna, S., Governato, F., Lake, G., Quinn, T., Stadel, J., & Tozzi, P. 1999, *ApJ*, 524, L19
- Muñoz, R. R., Carlin, J. L., Frinchaboy, P. M., Nidever, D. L., Majewski, S. R., & Patterson, R. J. 2006, *ApJ*, 650, L51
- Muñoz, R. R., Majewski, S. R., & Johnston, K. V. 2008, *ApJ*, 679, 346
- Oh, K. S., Lin, D. N. C., & Aarseth, S. J. 1995, *ApJ*, 442, 142
- Odenkirchen, M., et al., 2003, *AJ*, 126, 2385
- Peñarrubia, J., Navarro, J. F., & McConnachie, A. W. 2008, *ApJ*, 673, 226
- Peñarrubia, J., Navarro, J. F., McConnachie, A. W., & Martin, N. F. 2009, *ApJ*, 698, 222
- Piatek, S., & Pryor, C. 1995, *AJ*, 109, 1071
- Plummer, H. C. 1911, *MNRAS*, 71, 460
- Press, W. H., Flannery, B. P., Teukolsky, S. A., & Vetterling, W. T. 1988, *Numerical recipes in C: the art of scientific computing* (New York, NY, USA: Cambridge University Press)
- Read, J. I., Wilkinson, M. I., Evans, N. W., Gilmore, G., & Kleyna, J. T. 2006, *MNRAS*, 367, 387
- Ricotti, M., Gnedin, N. Y., & Shull, J. M. 2008, *ApJ*, 685, 21
- Rockosi, C. M. et al. 2002, *ApJ*, 124, 349
- Rutledge, G. A., Hesser, J. E., Stetson, P. B., Mateo, M., Simard, L., Bolte, M., Friel, E. D., & Copin, Y. 1997, *PASP*, 109, 883 *ApJ*, 124, 349
- Sakamoto, T., & Hasegawa, T.. 2006, *ApJ*, 653, L29
- Salpeter, E. E. 1955, *ApJ*, 121, 161
- Sand, D. J., Olszewski, E. W., Willman, B., Zaritsky, D., Seth, A., Harris, J., Piatek, S., & Saha, A. 2009, *ApJ*, 704, 898
- Simon, J. D., & Geha, M. 2007, *ApJ*, 670, 313
- Stetson, P. B. 1993, in *IAU Colloq. 136, Stellar Photometry, Current Techniques and Future Developments*, ed. C. J. Butler & I. Elliot (Cambridge: Cambridge Univ. Press), 291

Stetson, P. B. 1994, *PASP*, 106, 250

Strigari, L. E., Koushiappas, S. M., Bullock, J. S., Kaplinghat, M., Simon, J. D., Geha, M.,
& Willman, B. 2008, *ApJ*, 678, 614

Walsh, S. M., Willman, B., Sand, D., Harris, J., Seth, A., Zaritsky, D., & Jerjen, H. 2008,
ApJ, 688, 245

Walsh, S. M., Willman, B., & Jerjen, H. 2009, *AJ*, 137, 450

Willman, B. et al. 2005a, *AJ*, 129, 2692

Willman, B. et al. 2005b, *ApJ*, 626, L85

York, D. G. et al. 2000, *AJ*, 120, 1579

Zucker, D. B. et al. 2006a, *ApJ*, 643, L103

Zucker, D. B. et al. 2006b, *ApJ*, 650, L41

Table 1. Structural Parameters for both ComBer and UMa II

Parameter	Mean Coma Berenices	Uncertainty	Mean Ursa Major II	Uncertainty
$\alpha_{0,exp}$ (h m s)	12:26:59.00	$\pm 13''$	08:51:29.86	$\pm 27''$
$\delta_{0,exp}$ (d m s)	+23:54:27.2	$\pm 8''$	+63:07:59.2	$\pm 7''$
$r_{h,exp}$ (arcmin)	5.8	± 0.3	14.1	± 0.3
$r_{h,exp}$ (pc)	74	± 4	123	± 3
$r_{h,P}$ (arcmin)	5.9	± 0.3	13.9	± 0.3
$r_{h,P}$ (pc)	76	± 4	122	± 3
ϵ_{exp}	0.36	± 0.04	0.50	± 0.02
θ_{exp} (degrees)	−67.0	± 3.6	−74.8	± 1.7
$N_{*,exp}$	735	± 22	1335	± 35
r_c (arcmin)	4.2	± 0.5	10.8	± 0.8
r_c (pc)	54	± 6	94	± 7
r_t (arcmin)	27.9	± 3.4	64.2	± 2.8
r_t (pc)	355	± 43	560	± 24
M_V^a (Salpeter)	−3.8	± 0.6	−3.9	± 0.5
M_V^a (Chabrier)	−3.8	± 0.6	−4.0	± 0.6

^aUsing a distance of 44 and 30 kpc for ComBer and UMa II respectively, from Martin et al. (2008)

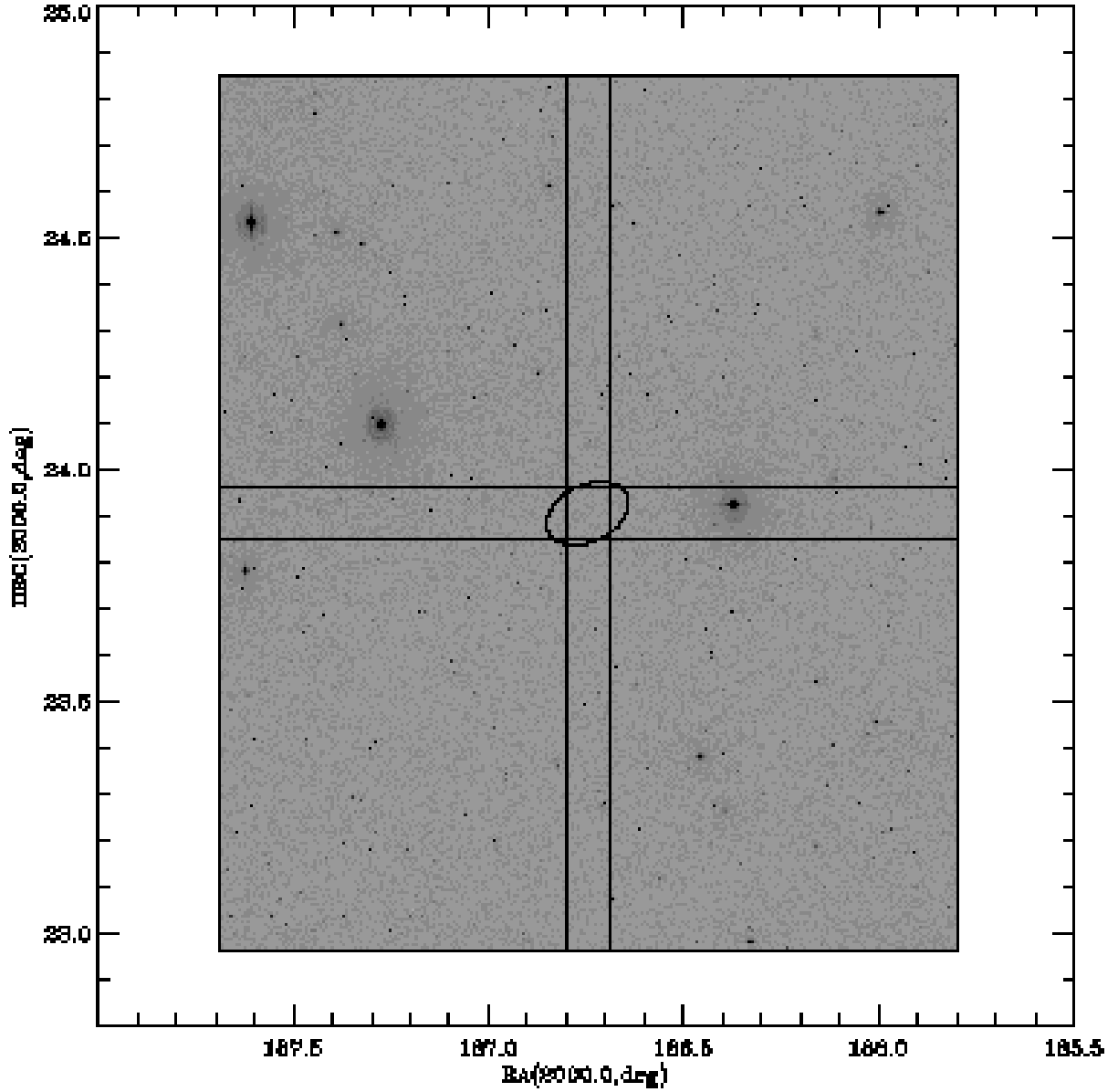


Fig. 1.— Schematic view of our photometric coverage for ComBer. We observed four different fields with MegaCam covering roughly $2 \times 2 \text{ deg}^2$ centered on the dSph galaxy. Here, the ellipse represents the half-light radius derived by Martin et al. (2008). A similar observing pattern was used for UMa II but for a total area of $1.4 \times 2 \text{ deg}^2$.

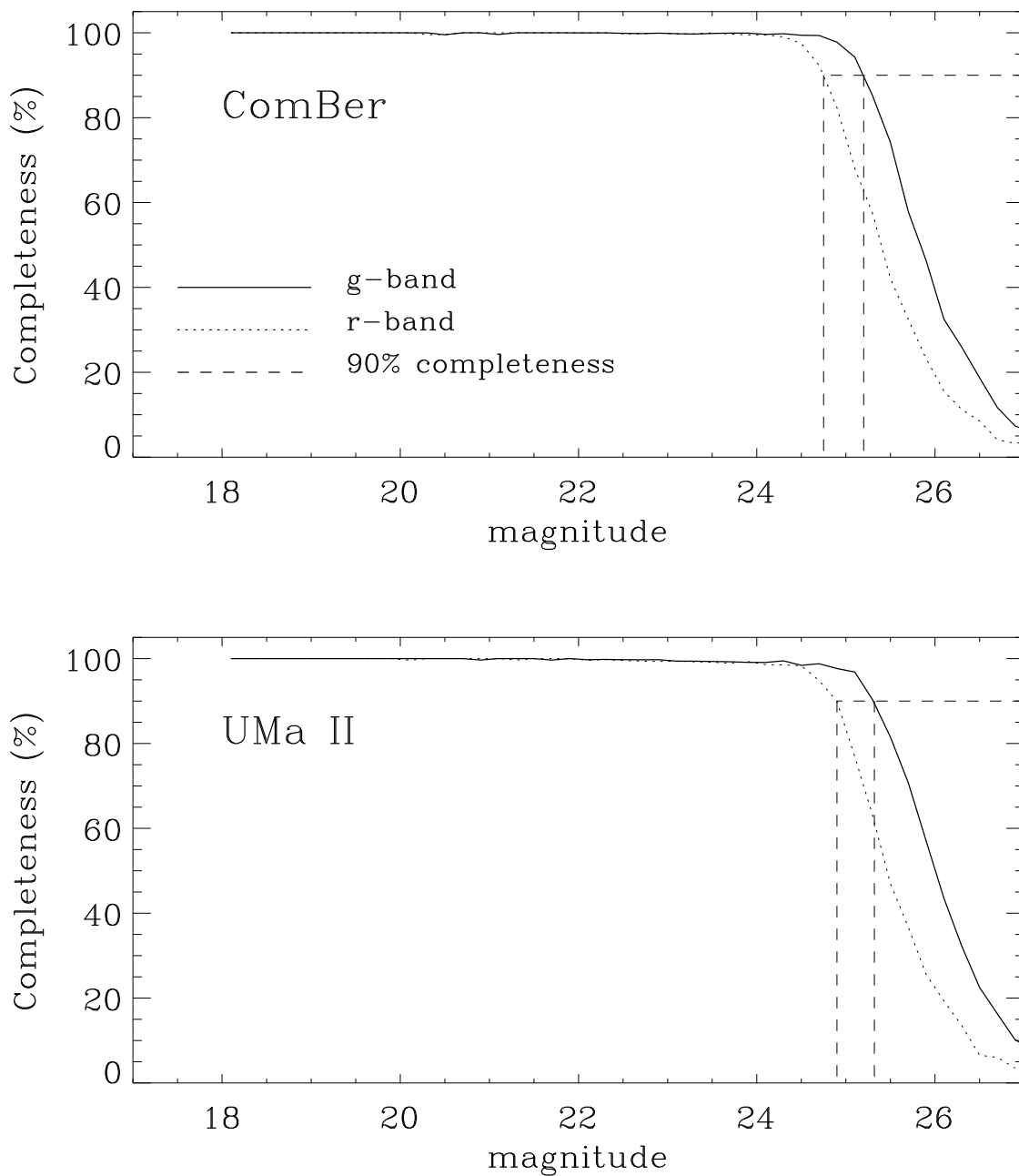


Fig. 2.— Completeness levels as a function of magnitude for our shallowest field in ComBer (upper panel) and in UMa II (lower panel). Solid and dotted lines represent the completeness levels as a function of g and r magnitude respectively. The dashed lines mark the 90% completeness levels, corresponding to $g = 25.2$ and $r = 24.75$ in the case of ComBer and $g = 25.4$ and $r = 24.9$ for UMa II (See text for further discussion).

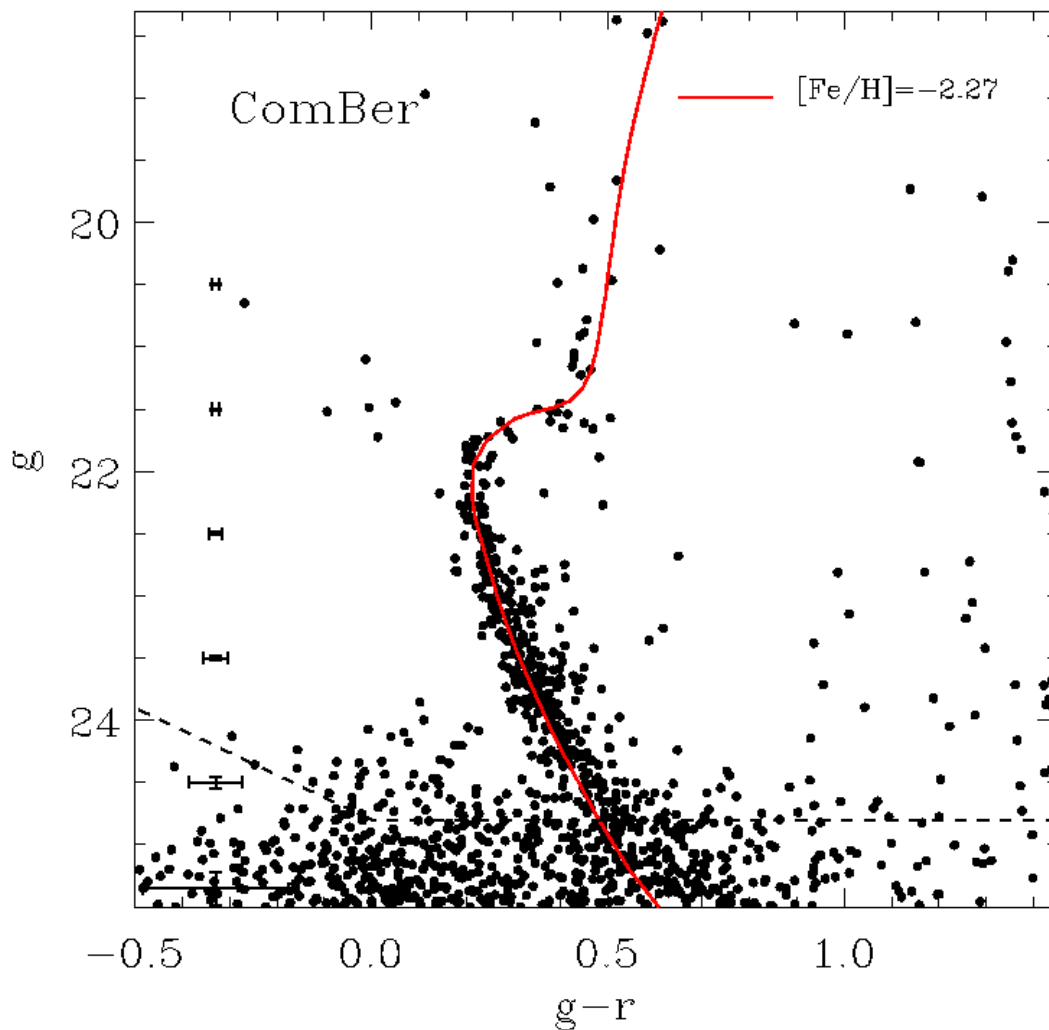


Fig. 3.— Color Magnitude Diagram for the inner region ($r < 6'$) of ComBer. The dashed lines mark the 90% completeness level after χ and *sharp* cuts have been applied to remove non-stellar objects. As it can be seen, our CFHT photometry reaches at least three magnitudes below the main sequence-turn-off of ComBer. We have complemented our photometry with SDSS data for $g > 20$. The error bars to the left were determined from the artificial star tests and represent the standard deviation of a Gaussian function fitted to the error distribution as a function of magnitude. A theoretical isochrone for a 13 Gyr old, $[\text{Fe}/\text{H}]=-2.27$ population is shown with a solid red line (from Girardi et al. 2004).

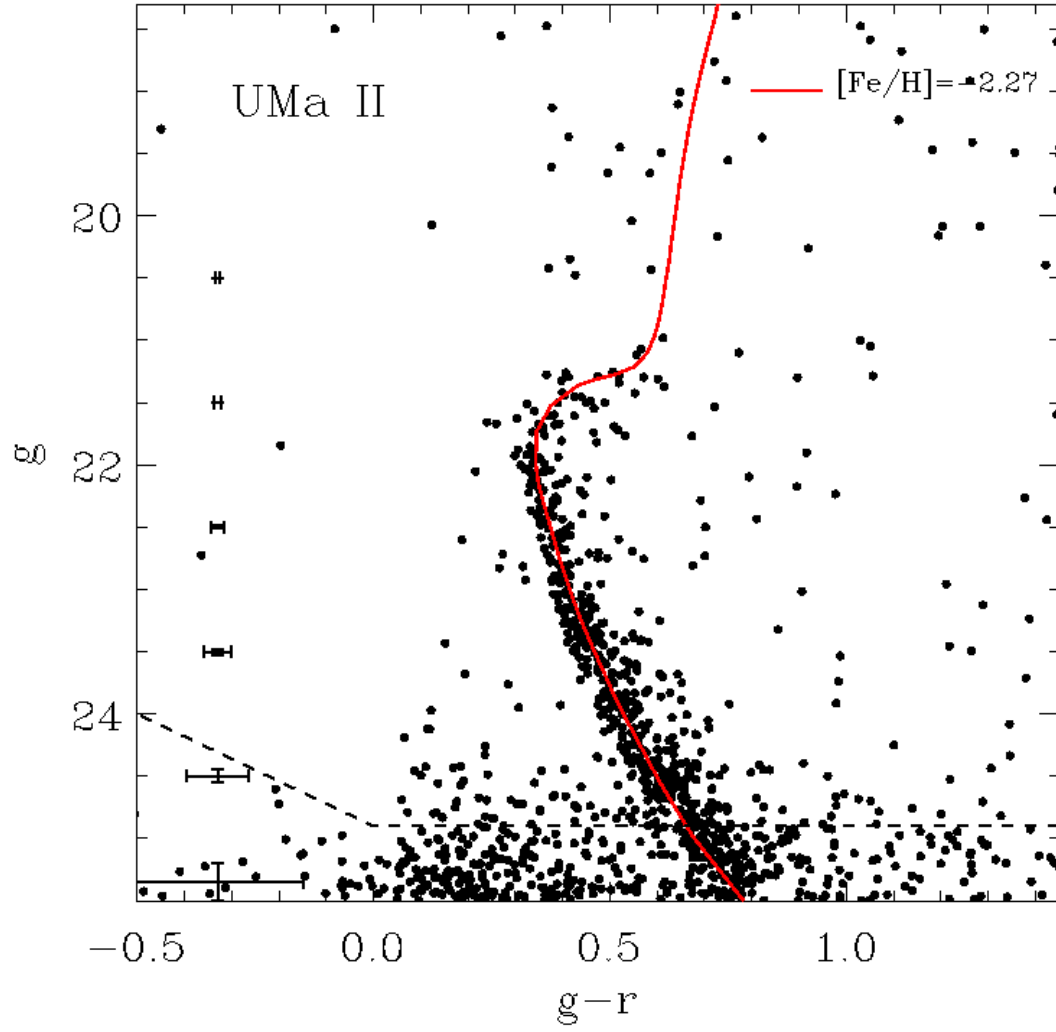


Fig. 4.— Similar to Figure 3 but for UMa II.

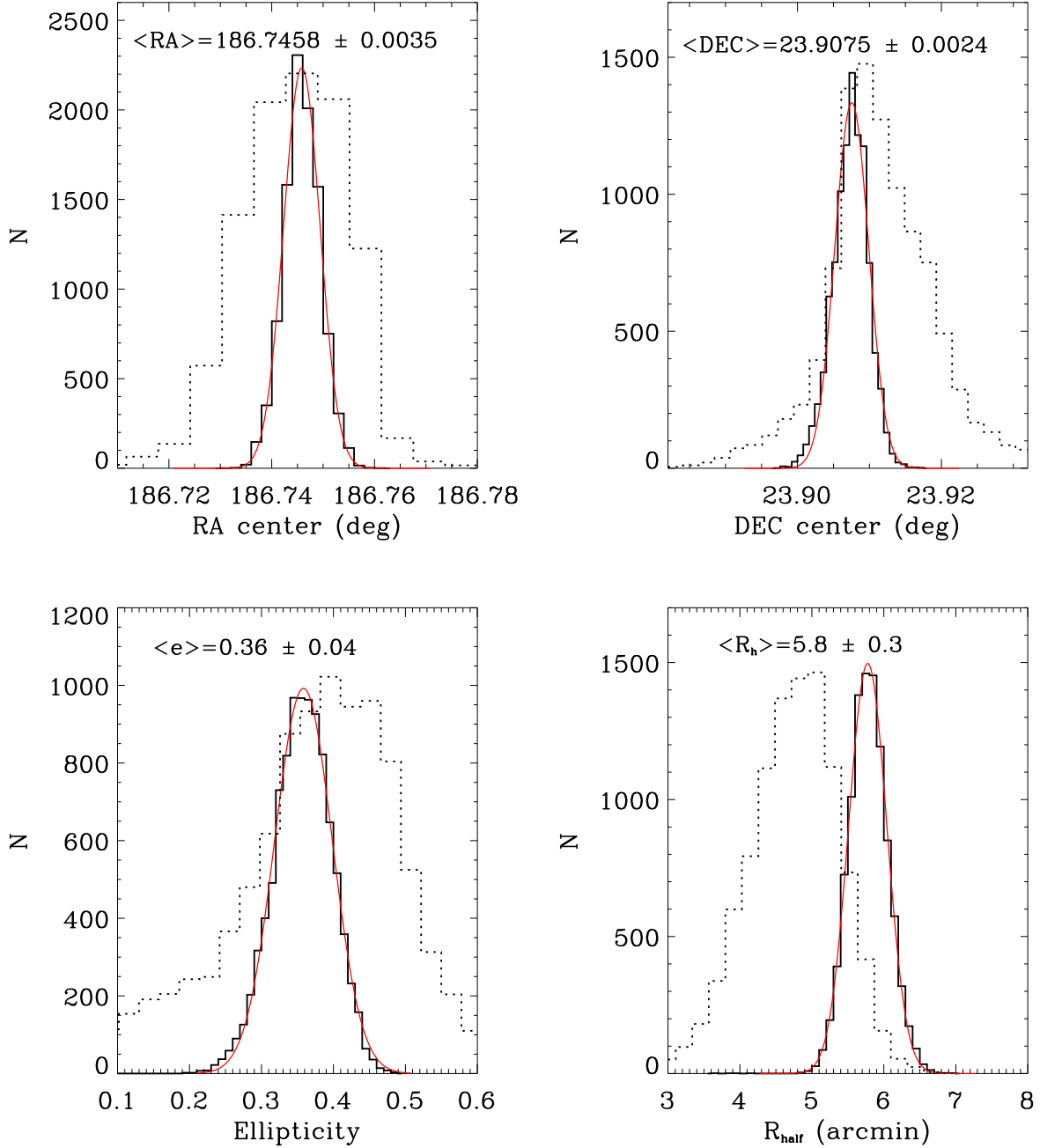


Fig. 5.— Comparison between structural parameters for ComBer derived by applying our ML method to both the CFHT and SDSS photometry. Solid histograms represent all 10,000 bootstrap realizations for the CFHT data while dotted histograms show the same but for SDSS data. The solid red curves show the best-fitted Gaussians to the CFHT histograms.

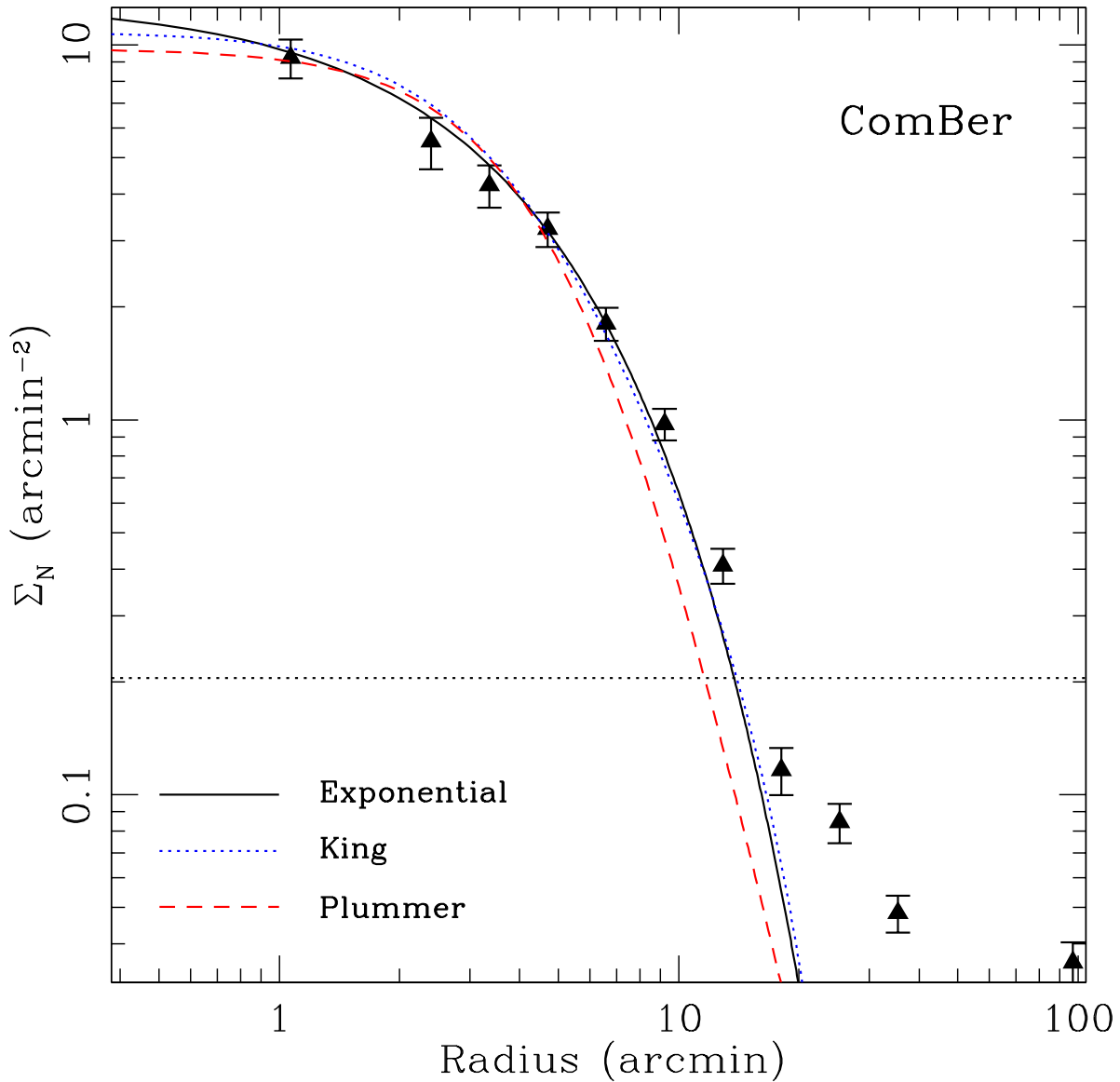


Fig. 6.— Background-subtracted number density profile for ComBer. The densities are calculated in elliptical annuli using the derived structural properties. Error bars were derived assuming Poisson statistics. The horizontal dotted line shows the level of the subtracted background. Solid (black), dotted (blue) and dashed (red) lines represent the best exponential, King and Plummer profiles respectively.

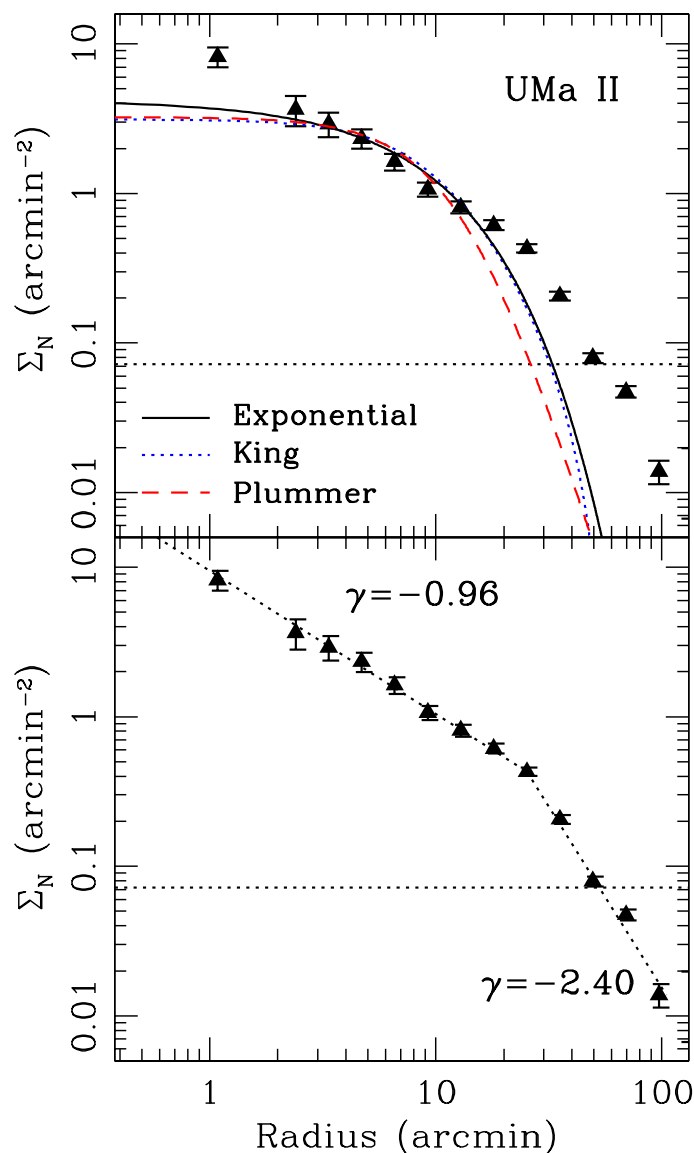


Fig. 7.— *Upper panel:* similar to Figure 6, but for UMa II. Note that neither profile represents a good fit to the observed data points. *Lower panel:* background subtracted number density profile of UMa II where the data points have been fitted with two power laws. These lines represent a much better visual fit to the data points than the density profiles used to derive UMa II’ structural parameters.

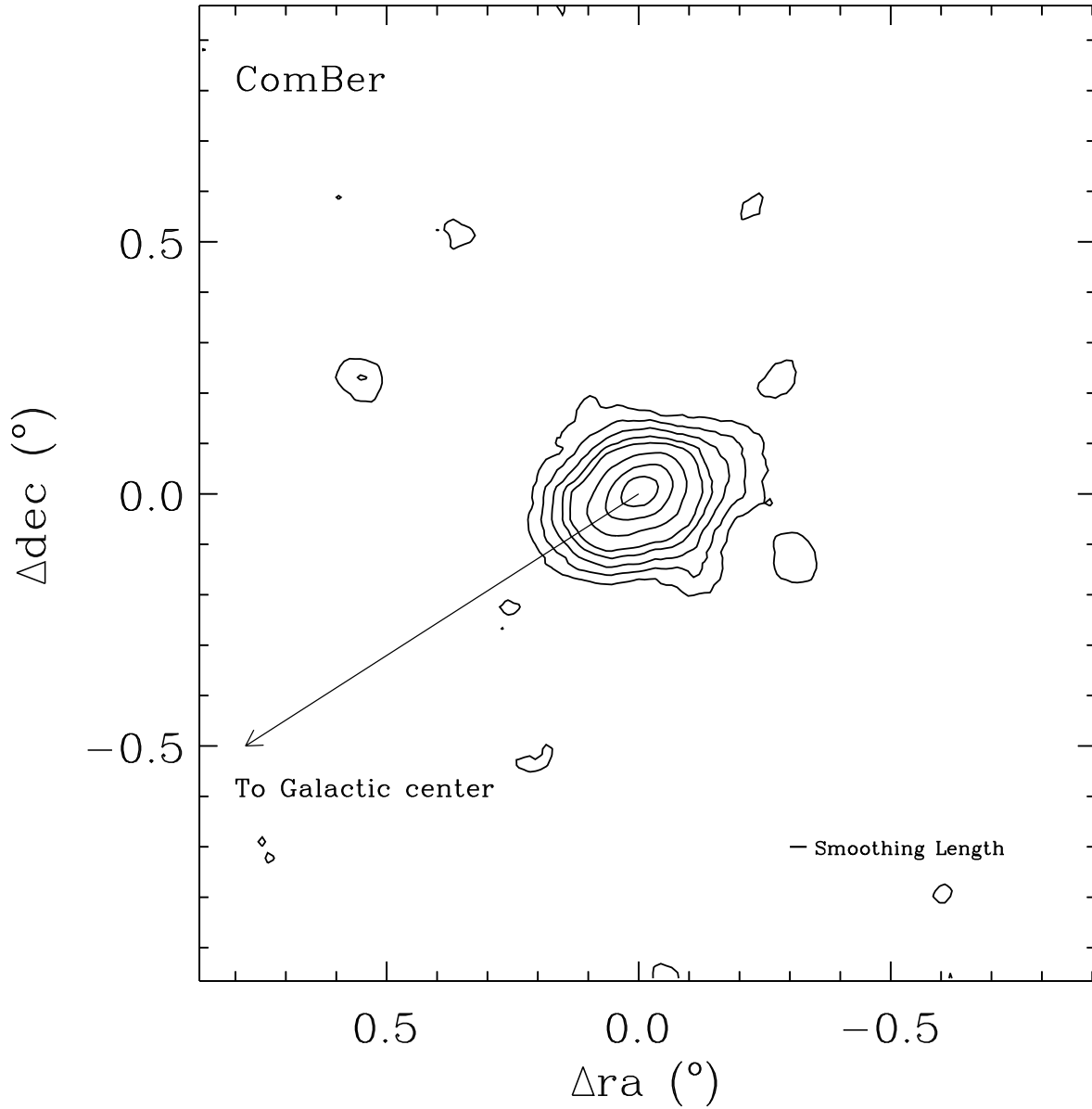


Fig. 8.— Isodensity contour map for ComBer. The contours represent 3, 6, 10, 15, 20, 35, 55 and 75σ above the mean density measured away from the main body of ComBer. The solid line shows the direction toward the Galactic center. The smoothing scale length of $2'$ is also indicated in the figure.

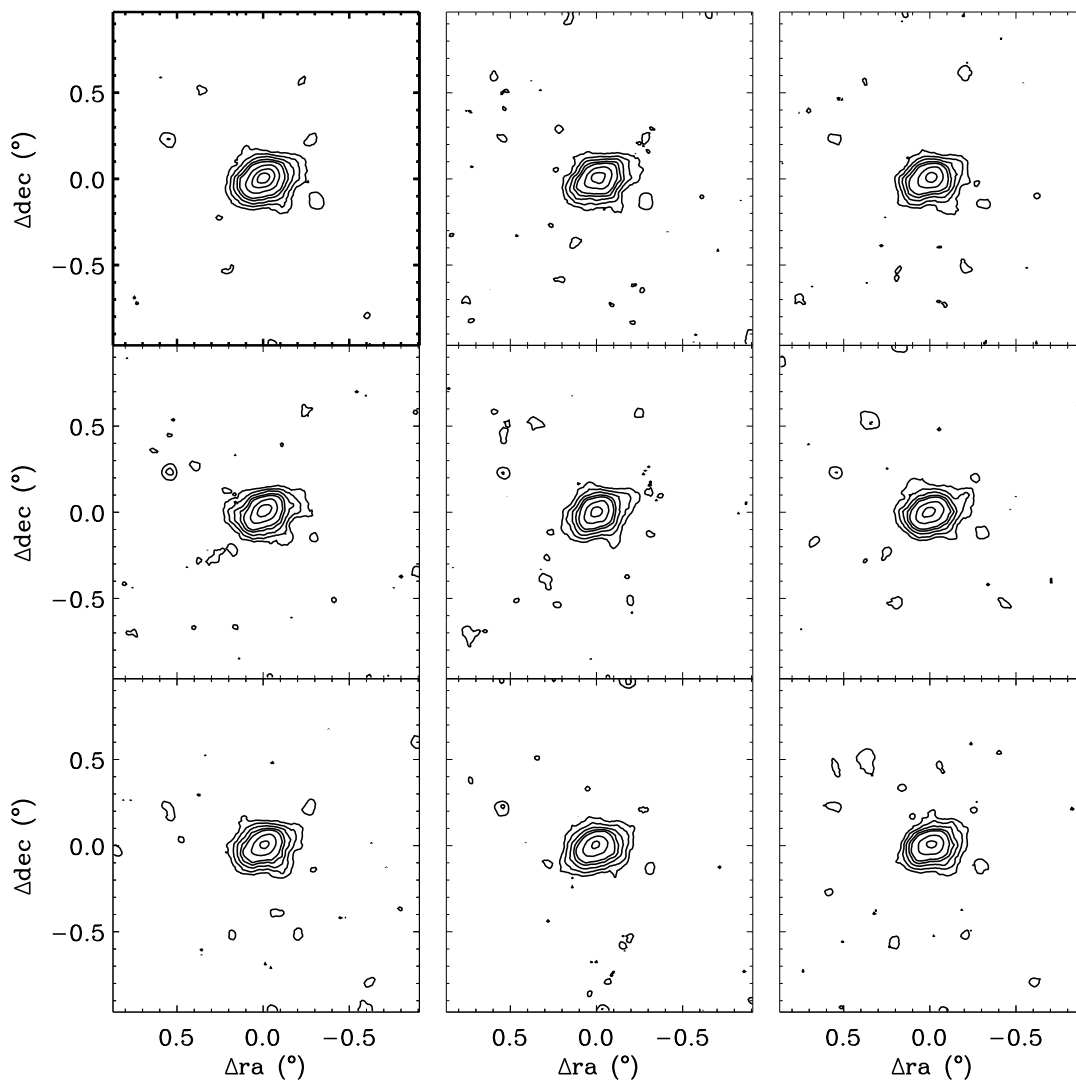


Fig. 9.— Isodensity contour maps for eight random bootstrap realizations of our photometric data for ComBer. The upper left panel (thicker axis) shows the contours for the actual data. As in Figure 8, we show 3, 6, 10, 15, 20, 35, 55 and 75σ above the mean density. While the lowest 3σ contours are not statistically significant, all more significant contours are well established with these data.

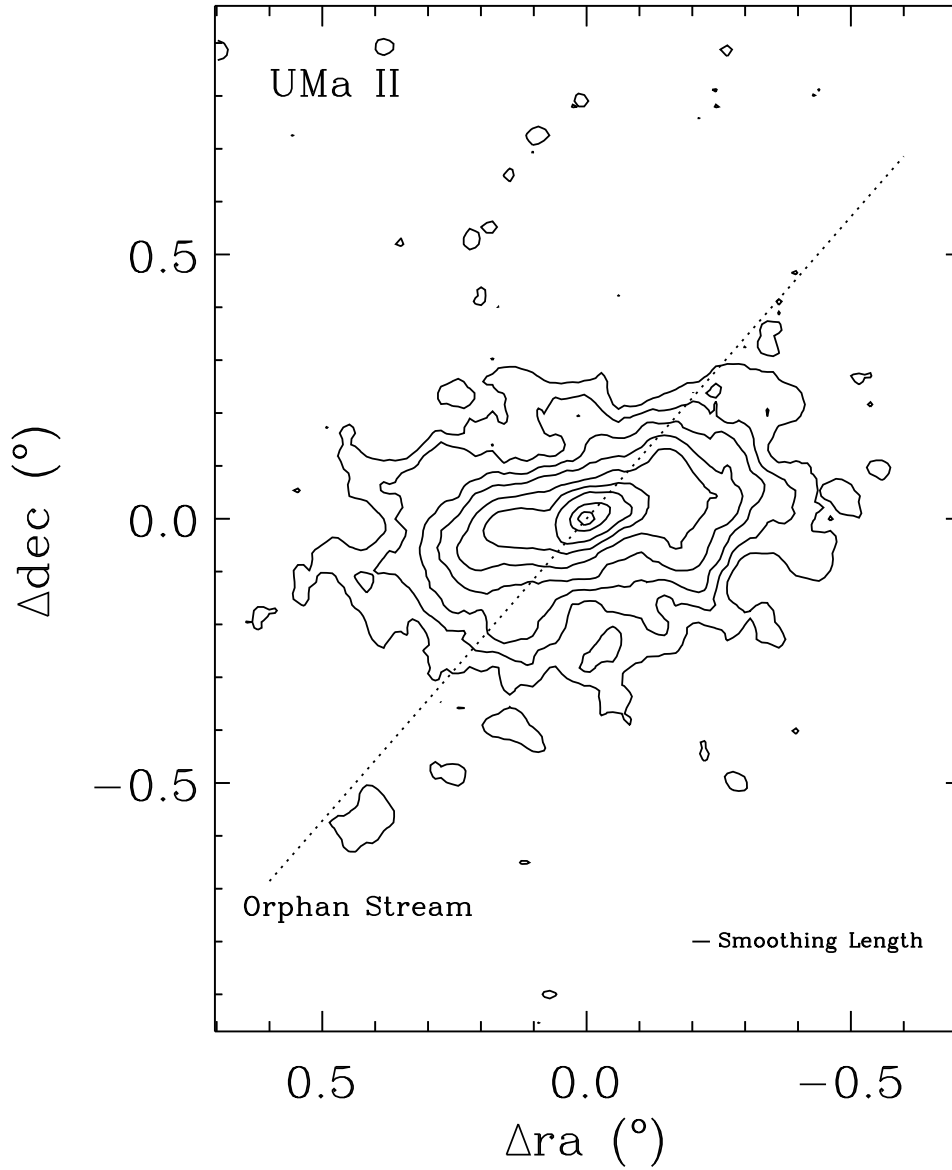


Fig. 10.— Isodensity contour map for UMa II. The contours in this case represent 3, 6, 10, 16, 26, 38, 55 and 70σ above the density measured in regions away from UMa II. The solid line marks the direction of the orbit derived by Fellhauer et al. (2007) assuming that UMa II is associated with the Orphan Stream. As in Figure 8, the smoothing scale length is shown for reference.

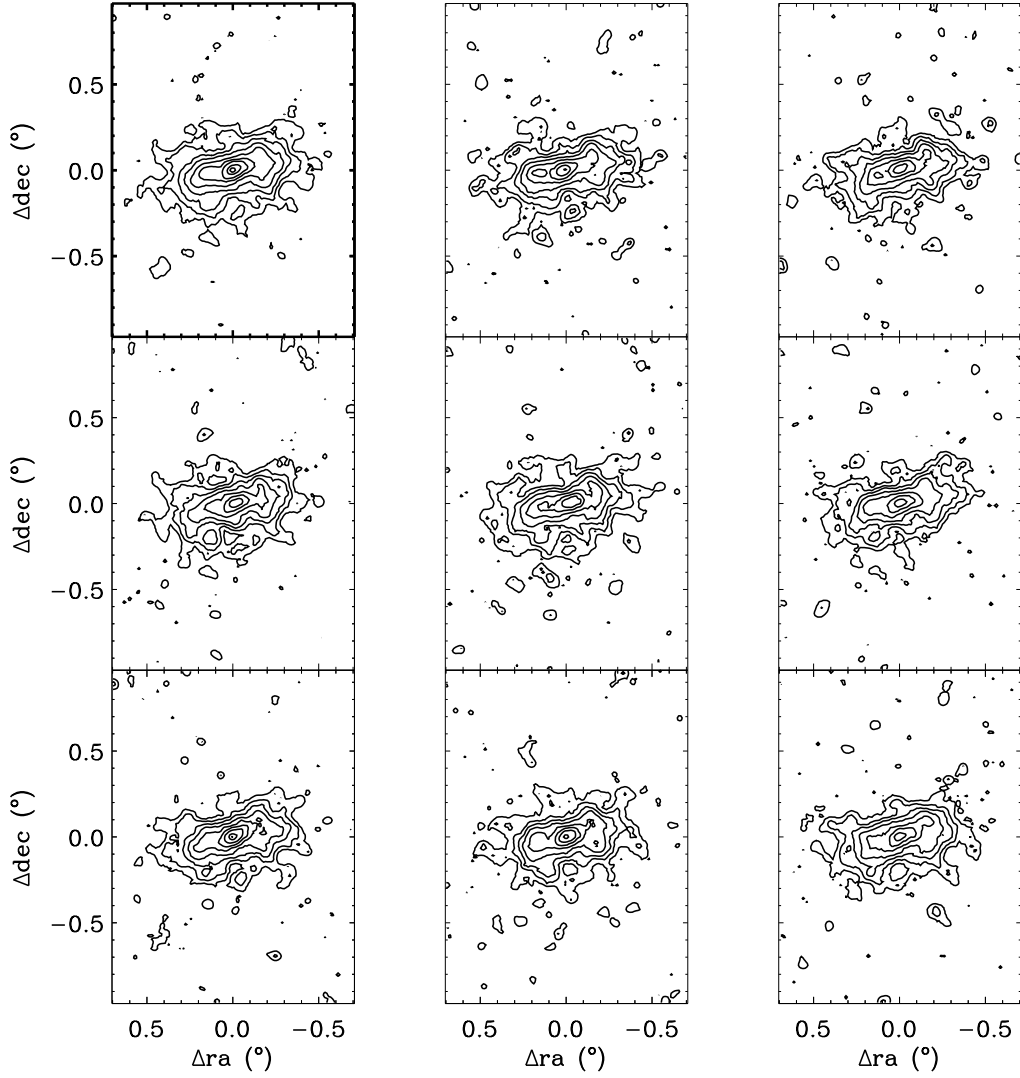


Fig. 11.— Similar to Figure 9 but for UMa II. The contours shown are similar to Figure 10, i. e., $3, 6, 10, 16, 26, 38, 55$ and 70σ above the mean density.